WILEY-VCH

ADVANCED OPTICAL MATERIALS

Research Article | Full Access

Personal Solar UV Monitoring based on Photoinduced Electron Transfers in Luminescent Materials

Zetian Yang, Jonas J. Joos, Jieqi Hu, David Van der Heggen, Tim Pier, Maxime Delaey, Henk Vrielinck, Thomas Jüstel, Philippe F. Smet, Dirk Poelman

First published: 15 May 2023 | https://doi.org/10.1002/adom.202300733

Personal Solar Ultraviolet Monitoring based on Photoinduced Electron Transfers in Luminescent Materials

Zetian Yang, Jonas J. Joos, Jieqi Hu, David Van der Heggen,* Tim Pier, Maxime Delaey, Henk Vrielinck, Thomas Jüstel, Philippe F. Smet, and Dirk Poelman**

Z. Yang, Dr. J. J. Joos, J. Hu, Dr. D. Van der Heggen, M. Delaey, Prof. P. F. Smet, Prof. D. Poelman
LumiLab, Department of Solid State Sciences, Ghent University, Krijgslaan 281-S1, Ghent B-9000, Belgium
E-mail: jonas.joos@ugent.be; david.vanderheggen@ugent.be; dirk.poelman@ugent.be

T. Pier, Prof. T. Jüstel
Department of Chemical Engineering, Münster University of Applied Sciences,
Stegerwaldstrasse 39, Steinfurt D-48565, Germany

Prof. H. Vrielinck
Electron Magnetic Resonance Group, Department of Solid State Sciences, Ghent University,
Krijgslaan 281-S1, Ghent B-9000, Belgium

Keywords: luminescent materials, light dosimeter, photo-induced electron transfer, personal solar ultraviolet monitor

The spectrally-selective monitoring of doses of ultraviolet and visible light is crucial in numerous applications like photodynamic therapy and personal solar ultraviolet detection, due to the specific irradiation impact of light with different wavelengths and doses. Herein an approach to design wavelength-specific integrating light dosimeters is demonstrated based on photo-induced redox processes of certain lanthanides in phosphate compounds. Systematic experiments reveal that the reduction process is induced through ligand-to-metal charge transfer excitation while the oxidation process is achieved upon excitation of either the involved hole traps or $4f^N$-$4f^{N-1}5d^1$ transitions of the created divalent dopants. These processes are rationalized in multi-electron energy level diagrams for local electron transfer. The dose and wavelength dependent redox processes allow for selective ultraviolet and visible light dosimetry and the spectral sensitivity of the dosimeter can be tailored by manipulating the dopant or the host. Particularly, the spectral sensitivity of $Ba_{2.99}Eu_{0.01}(PO_4)_2$ better matches the erythemal action

spectrum of human skin than that of currently-used benchmark polysulphone dosimeters, making it ideally suitable for personal solar ultraviolet radiation monitoring. These findings open the door to design wavelength-tunable light dosimeters according to the requirements of envisioned applications and are expected to benefit a wide range of luminescent functional devices.

1. Introduction

Natural and anthropogenic light sources are utilized in multiple fields like general lighting, medical therapy and precision agriculture.[1-3] Exposure to controlled quantities can provide certain benefits, while a sequence of risks can also be induced upon overexposure. Specifically, UVC (100 - 280 nm) irradiation is widely used in industrial processes and hospitals to kill microorganisms,[4] a moderate dose of UVB (280 - 315 nm) irradiation is essential for the production of vitamin D through promoting carbon-carbon bond cleavage,[5] and ultraviolet irradiation therapy is promising in e.g. the management of obesity and addiction.[6] However, the associated risks such as skin pathology e.g., dark stains, aging, and cancer, macular degeneration and circadian rhythm disorder will manifest when the irradiation dose exceeds certain thresholds.[7] Excessive ultraviolet exposure has become the leading cause of skin cancer.[8] Apart from the dose-dependent characteristic, the effect of exposure to radiation also strongly depends on the wavelength. An example is the erythemal action spectrum of human skin for which 280 nm light is nearly twenty times more damaging to the skin than 310 nm light, even if both of them belong to UVB.[9] Similar cases are also encountered in photodynamic therapy, in the conservation of art and in precision agriculture.[10-12] The effects of light irradiation on healing lesions, degrading pigments or regulating plant growth and physiology are also strongly dependent on the wavelength.[2, 10-12] In this sense, the development of wavelength-specific light dosimeters that can not only measure the cumulative dose but also properly match the action spectrum of irradiated targets is of paramount importance for the effective use of light in medical diagnosis, for the preservation of dyed artworks or for preventive health care.

Light dosimeters that can quantify incident doses can be achieved based on either active detectors or passive detectors.[13-15] Active detectors mainly rely on the photovoltaic effect or the photoconductive effect of semiconductors such as silicon, metal oxides or III-V nitrides that convert incident light into electrical signals.[16-18] However, the underlying mechanism determines that such kind of detectors, in principle, respond to all photons with an energy higher than the associated absorption edge and thus lack the capability of spectrally-selective detection. Additionally, a power supply combined with real-time data processing or near-field

communication is required for active detectors to provide the integrated dose information.[19-22] This requirement inevitably makes them bulky and costly, and limits the operating lifetime, which is a nuisance for day-to-day dosimetry. A method to overcome these limitations is to develop a standalone passive dosimeter that can stably store the incident dose information during dosimetry followed by a subsequent readout upon external stimulus. The constant detection, battery-free operation and inexpensive characteristics make this type of dosimeter suitable for long-term monitoring of daily light exposure. Inspired by this, various passive light dosimeters based on photonic crystals, photodegradable dyes, minerals, transition metal oxides, hydrogel or metal-organic frameworks have been developed, in which the optical density or the luminescence intensity is proportional to the incident dose.[23-29] Despite these extensive efforts, most of these passive dosimeters are restricted to monitoring the dose of a monochromatic light source in addition to issues of poor stability or non-reusability. Therefore, the progress toward developing wavelength-specific light dosimeters is still limited and there have been no advanced approaches to guide the design of such dosimeters.[24, 28, 30] For example, the currently used dosimeter for personal solar ultraviolet monitoring is still the polysulphone of which the dosimetric capabilities were discovered by Davis *et al*. in 1976,[9] even though its spectral sensitivity only poorly matches the erythemal action spectrum of human skin which consequently requires a complex calibration and thus can generate large inaccuracies.[31] As a result, the quest for developing integrating light dosimeters that exhibit spectrally selective detection tailored to the needs of a specific application remains ongoing.

An alternative approach to light dosimetry relies on photo-induced electron transfers in inorganic luminescent materials. In these processes, it is the luminescence activator, i.e. a dopant, that undergoes a valence state change.[30, 32, 33] The incident dose is therefore encoded into the photoluminescence intensities of the dopant in its different valence states. Moreover, the wide choice of hosts and dopants provides the possibility to develop materials with different wavelength dependency of photo-induced electron transfer behavior. However, the limited understanding of the charge transfer processes in luminescent materials hinders their further exploration for wavelength-specific light dosimetry.

In this work, systematic optical spectroscopy and electron paramagnetic resonance experiments are presented for $Ba_{2.99}Ln_{0.01}(PO_4)_2$ (Ln = Eu, Sm, or Yb) and $Sr_{2.99}Sm_{0.01}(PO_4)_2$ to reveal the photo-induced charge transfer processes. It is shown that the photo-reduction process from Ln^{3+} to Ln^{2+} can be induced through a ligand-to-metal charge transfer, while the obtained Ln^{2+} can be re-oxidized by optical excitation of the trapped holes or upon $4f^N$-$4f^{N-1}5d^1$ excitation of the generated Ln^{2+} ions. The wavelength and dose dependency of the reversible

valence change in combination with the stability of the trapped state makes these materials highly suited for wavelength-specific dosimetry of ultraviolet to visible light. The dose is read out optically from the absolute luminescence intensity of Ln^{2+} or Ln^{3+}, or from the luminescence intensity ratio between Ln^{2+} and Ln^{3+} after prior calibration. The proposed approach allows to tune the dosimeter response by sensibly choosing the dopant and host to exploit the systematic behavior of the photo-induced redox processes. This opens the door to design wavelength-specific integrating light dosimeters according to the requirements of envisioned applications.

2. Results and Discussion

2.1. Photoluminescence Spectra

The room-temperature photoluminescence spectra of the prepared phosphates are presented in **Figure 1**. Before irradiation, the typical photoluminescence emission (PL) spectra and photoluminescence excitation (PLE) spectra of Ln^{3+} were observed for all samples synthesized in air (see Figure 1a-1d), indicating that the Ln ions were incorporated into the host matrix in their trivalent state. Specifically, the emission spectrum of $Ba_{2.99}Eu_{0.01}(PO_4)_2$ consists of the intraconfigurational $4f^6$ ($^5D_0 \rightarrow {}^7F_J$ (J = 0, 1, 2, 3, 4)) transitions of Eu^{3+}. The emission lines in $Ba_{2.99}Sm_{0.01}(PO_4)_2$ and $Sr_{2.99}Sm_{0.01}(PO_4)_2$ are assigned to the intraconfigurational $4f^5$ ($^4G_{5/2} \rightarrow {}^6H_J$ (J = 5/2, 7/2, 9/2, 11/2)) transitions of Sm^{3+} and the near-infrared emission in $Ba_{2.99}Yb_{0.01}(PO_4)_2$ is assigned to the intraconfigurational $4f^{13}$ ($^2F_{5/2} \rightarrow {}^2F_{7/2}$) transition of Yb^{3+}. Meanwhile, the associated excitation spectra of Eu^{3+}, Sm^{3+} and Yb^{3+} are also shown. In addition, excitation spectra in the vacuum ultraviolet (VUV) range from 120 to 375 nm were recorded to reveal the excitation bands in the deep ultraviolet range (see Figure S1a-S1c). All excitation spectra show a combination of two broad bands in the deep ultraviolet range and sharp lines in the near ultraviolet range. The sharp excitation lines can be assigned to the previously discussed intraconfigurational *f-f* transitions of the respective trivalent lanthanide ions. The broad bands in the 200 nm to 300 nm range are caused by the respective ligand-to-metal charge transfers (LMCT, O^{2-}-$Ln^{3+} \rightarrow O^{-}$-$Ln^{2+}$) and thus are essential for the investigation of the photo-induced redox processes. Finally, the bands between 150 nm and 200 nm can be assigned to the tetrahedral PO_4^{3-} moiety. These ortho-phosphate units are known to show strong absorption bands in the VUV range and similar results have previously been reported for $Sr_3(PO_4)_2$ doped with different lanthanide ions.[34]

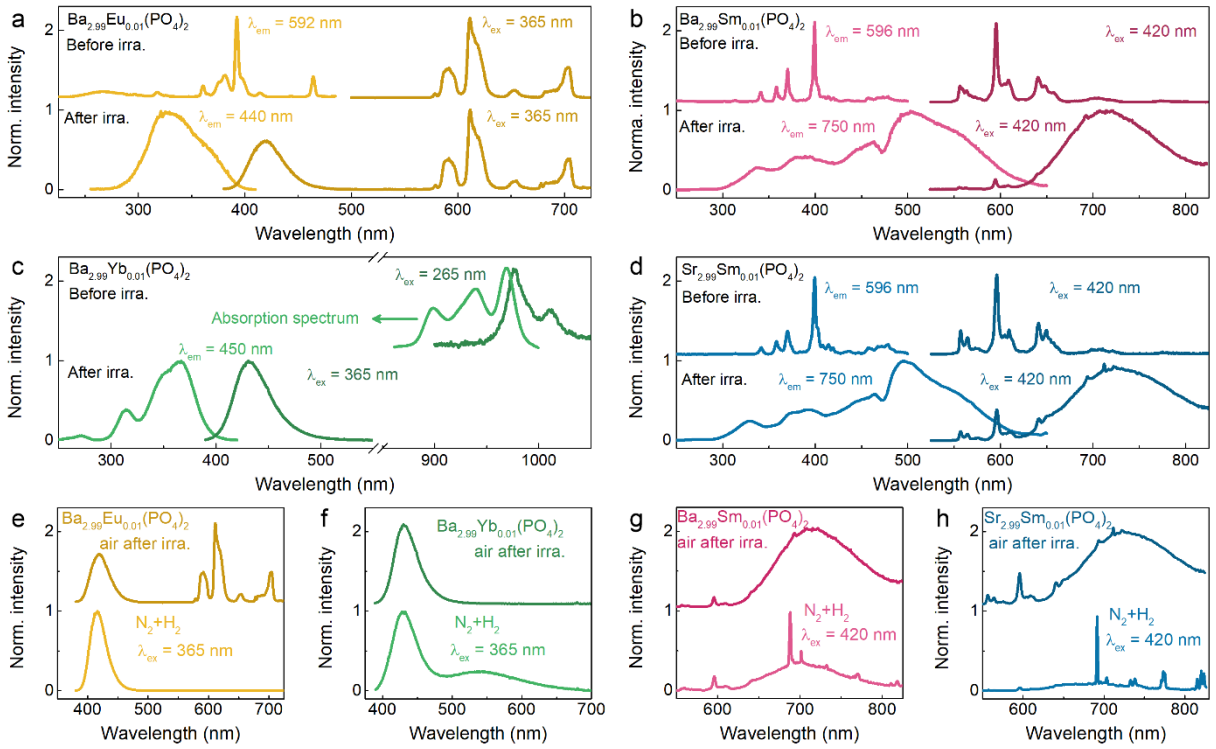

Figure 1. Photoluminescence properties of the synthesized materials. The photoluminescence excitation and emission spectra of a) $Ba_{2.99}Eu_{0.01}(PO_4)_2$, b) $Ba_{2.99}Sm_{0.01}(PO_4)_2$, c) $Ba_{2.99}Yb_{0.01}(PO_4)_2$ and d) $Sr_{2.99}Sm_{0.01}(PO_4)_2$ synthesized in air before and after 215 nm irradiation. For $Ba_{2.99}Yb_{0.01}(PO_4)_2$ synthesized in air, the absorption spectrum was adopted to reflect the photoluminescence excitation characteristics. The photoluminescence emission spectra of e) $Ba_{2.99}Eu_{0.01}(PO_4)_2$, f) $Ba_{2.99}Yb_{0.01}(PO_4)_2$, g) $Ba_{2.99}Sm_{0.01}(PO_4)_2$ and h) $Sr_{2.99}Sm_{0.01}(PO_4)_2$ synthesized in air after 215 nm irradiation and synthesized in N_2+H_2. The used excitation and monitored emission wavelengths are indicated in the graphs.

After 215 nm irradiation, a new emission band related to Ln^{2+} appears in all Ln^{3+} doped samples prepared in air. For the Eu and Yb-doped compounds, only a new broad emission band is detected, which can be assigned to the $4f^6 5d^1 \rightarrow 4f^7$ and $4f^{13} 5d^1 \rightarrow 4f^{14}$ transitions, respectively. For the Sm-doped compounds, both a broad emission band and sharp emission lines are observed, which originate from the $4f^5 5d^1 \rightarrow 4f^6$ and $4f^6 \rightarrow 4f^6$ ($^5D_0 \rightarrow {}^7F_J$ (J = 0, 1, 2, 3, 4)) transitions in Sm^{2+}, respectively, due to the crossover of the excited $4f^5 5d^1$ state and the $4f^6$ ($^5D_0$) state. Meanwhile, the corresponding PLE spectrum of Ln^{2+} was also obtained by monitoring the emission peak of Ln^{2+}. The presence of these new emissions shows that a fraction of the Ln^{3+} ions is reduced to Ln^{2+} upon 215 nm irradiation. This was further confirmed by comparing the spectra to the nearly identical PL spectra of samples directly synthesized under reducing conditions in N_2+H_2 (see Figure 1e-1h). However, small differences between the PL spectra can be found by taking a closer look, especially for the Yb- and Sm-doped

compounds (see Figure 1f-1h). The PL spectrum of $Ba_{2.99}Yb_{0.01}(PO_4)_2$ prepared in air after 215 nm irradiation (called photo-reduced sample hereafter), for example, only exhibits the emission band centered at 428 nm while it lacks the relatively weak emission band centered at 540 nm which is present in the spectrum of the sample synthesized in N_2+H_2 (see Figure 1f). For $Ba_{2.99}Yb_{0.01}(PO_4)_2$ synthesized in N_2+H_2, an excitation wavelength dependency of the shape of the PL spectra was found (Figure S1d), while such a behavior was not observed for photo-reduced $Ba_{2.99}Yb_{0.01}(PO_4)_2$ (Figure S1e). A similar phenomenon is also observed in Sm-doped compounds (Figure S1f and S1g). $Ba_3(PO_4)_2$ has a rhombohedral crystal structure in *R*-3*m* space group, where Ba^{2+} occupies two inequivalent sites with a ten- and a twelve-fold coordinated oxygen-polyhedron, respectively.[35] These observations indicate that Yb^{2+}/Sm^{2+} ions can occupy two different crystallographic sites when synthesized in N_2+H_2, while only one type of Yb^{2+}/Sm^{2+}-center can be obtained by irradiation-induced reduction. Such an site-dependent preferential reduction process was also confirmed in lanthanide-doped CaF_2 where only the lanthanides without a local charge-compensating defect could be photoreduced.[36]

For the Eu-doped samples a similar yet more subtle effect takes place. Electron paramagnetic resonance (EPR) measurements were performed to confirm the partial photoreduction of Eu in detail. As shown in Figure S2a, a strong EPR signal consisting of multiple broad lines, related to Eu^{2+} ions in two crystallographic sites, was observed for the sample synthesized in N_2+H_2. The corresponding signals from only one of the sites were detected for the photo-reduced sample, revealing that Eu ions are present in trivalent state when synthesized in air and that only a fraction of Eu^{3+} is converted to Eu^{2+} upon irradiation. Similar to the observation from PL for $Ba_{2.99}Yb_{0.01}(PO_4)_2$, EPR reveals that Eu^{3+} is photo-reducible in only one of the crystallographic sites. In $Ba_3(PO_4)_2$, both Ba^{2+} sites have axial symmetry. The set of broad lines in the EPR spectrum of the photo-reduced sample can be convincingly reproduced by assuming a single Eu^{2+} center with an axially symmetric spin Hamiltonian. The spectrum for this Eu^{2+} site is also present in the EPR spectrum of the sample synthesized N_2+H_2, but additional transitions for another Eu^{2+} spectrum with axially symmetric spin Hamiltonian occur, as is clear from the simulations in Figure S2b. To probe the site occupancy of Eu^{3+}-doped $Ba_3(PO_4)_2$ synthesized in air, low-temperature PL measurements were performed (see Figure S3). The observation of two lines (centered at 17337 cm^{-1} and 17265 cm^{-1}) for the non-degenerate $^5D_0 \rightarrow {}^7F_0$ transition reveals that Eu^{3+} ions occupy at least two different crystallographic sites when synthesizing in air.[37] Combined with the EPR results, it can indeed be concluded that only one-type of Eu^{3+} is reduced to Eu^{2+} upon photon irradiation.

2.2. Photo-induced Redox Processes

To provide a deeper understanding of photo-induced valence change processes, irradiation wavelength-dependent reduction and oxidation experiments were systematically carried out. For the reduction process, the sample was first brought in a state in which the largest fraction of Ln was oxidized before performing the reduction experiments at every selected wavelength. Similarly, for the photo-oxidation experiment at each wavelength, the sample was first illuminated to induce a maximal photoreduction of the Ln dopants. The results of the wavelength-dependent reduction and oxidation spectroscopy experiments are presented in Figure S4 - Figure S7 and Figure S8 - Figure S11, respectively. It is shown that a reversible valence change of $Ln^{2+} \leftrightarrow Ln^{3+}$ can be realized in all compositions upon alternating photon stimuli. Additionally, dose response curves, i.e. PL intensities as a function of integrated irradiated energy (in mJ), are also obtained (see Figure S12). These results show that some wavelengths are more efficient than others for the same composition, irrespective of the reduction process (see Figure S13) or the oxidation process (see Figure S14). To quantify the effectiveness of different wavelengths to induce the redox process, the photoluminescence intensity ratio between Ln^{2+} and Ln^{3+} ($I_{Ln^{2+}}/I_{Ln^{3+}}$) was calculated for Eu or Sm-doped compounds, while the absolute emission intensity of Yb^{2+} ($I_{Yb^{2+}}$) was used for $Ba_{2.99}Yb_{0.01}(PO_4)_2$ as it was difficult to record the PL spectra of Yb^{3+} and Yb^{2+} simultaneously due to the large spectral separation between both bands.

The normalized effectiveness for the reduction process as a function of irradiation wavelength is presented in **Figure 2a**, where the effectiveness is defined by the value change of $I_{Ln^{2+}}/I_{Ln^{3+}}$ or $I_{Yb^{2+}}$ after irradiation with fixed doses. It is shown that $Ba_{2.99}Eu_{0.01}(PO_4)_2$ can be reduced when the irradiation wavelength is shorter than 340 nm whereas this cut-off wavelength is shifted to higher energy by changing the chemical composition from $Ba_{2.99}Eu_{0.01}(PO_4)_2$ to $Ba_{2.99}Yb_{0.01}(PO_4)_2$, $Ba_{2.99}Sm_{0.01}(PO_4)_2$ or $Sr_{2.99}Sm_{0.01}(PO_4)_2$. By comparing the wavelengths and spectral shapes of the photo-reduction effectiveness with the PLE spectrum of the Ln^{3+} ions, a striking correspondence is found (solid line in Figure 2a). The LMCT band of the Ln^{3+} ion is also found in the photo-reduction effectiveness characteristic, revealing that the photo-reduced state can hence be reached via the LMCT. During the photo-reduction process, the Ln^{3+} ions act as electron trap and are converted to Ln^{2+}. Meanwhile, the holes are trapped at the involved defects (D^Q): D^Q is oxidized to D^{Q+1}. The chemical nature of this redox-active defect is unknown, although it is possible that it is the charge compensator which is created when substituting Ln^{3+} on a Ba^{2+} or Sr^{2+} site.

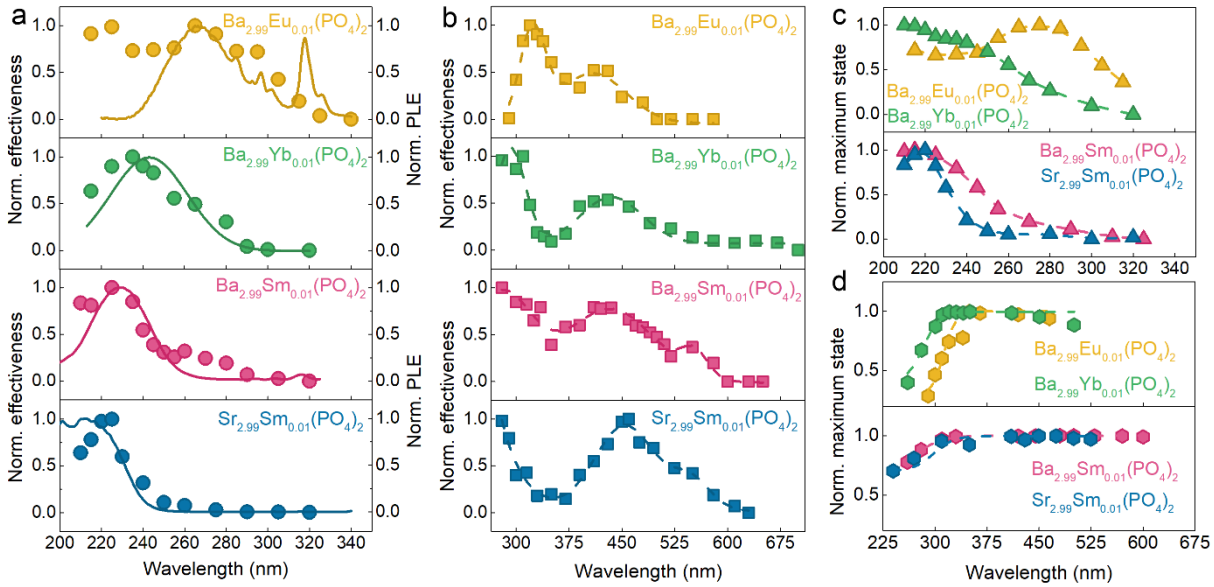

Figure 2. Wavelength-dependent reduction and oxidation processes of the samples synthesized in air. a) Effectiveness of different wavelengths for the reduction processes in $Ba_{2.99}Eu_{0.01}(PO_4)_2$ (yellow dot), $Ba_{2.99}Yb_{0.01}(PO_4)_2$ (green dot), $Ba_{2.99}Sm_{0.01}(PO_4)_2$ (red dot) and $Sr_{2.99}Sm_{0.01}(PO_4)_2$ (blue dot). The corresponding photoluminescence excitation spectra of Ln^{3+} (solid lines) are also given for comparison. b) Effectiveness of different wavelengths for the oxidation processes (the dashed lines are a guide to the eye). Irradiation wavelength-dependent c) maximum reduction effect and d) maximum oxidation effect (the dashed lines are a guide to the eye).

It is shown in Figure 2b that re-oxidation of the lanthanide ion can be achieved upon irradiation with a wide range of wavelengths. The effectiveness of the oxidation process was determined under illumination with small doses to ensure that no saturation effects had to be taken into account. The effectiveness of different wavelengths for the same composition and the cut-off wavelengths for different compositions are however slightly different. The response curves of $Ba_{2.99}Sm_{0.01}(PO_4)_2$ and $Sr_{2.99}Sm_{0.01}(PO_4)_2$ exhibit an additional band around 550 nm in comparison with those of $Ba_{2.99}Eu_{0.01}(PO_4)_2$ and $Ba_{2.99}Yb_{0.01}(PO_4)_2$. It can be expected that the oxidation process is induced via $4f^N$-$4f^{N-1}5d^1$ excitation of the metastable Ln^{2+} ion. A comparison between the PLE spectra of Ln^{2+} ions (see Figure 1a-1d) and the wavelength-dependent oxidation spectra (see Figure 2b) shows that the characteristic $4f^N$-$4f^{N-1}5d^1$ excitation indeed occurs for Eu^{2+}, Sm^{2+} and Yb^{2+}, but that this does not explain the entire spectral response for photo-oxidation. An additional broad band in the range of 350-500 nm is found for all $Ba_3(PO_4)_2$, irrespective of the dopant. For $Sr_3(PO_4)_2$, a similar band is found, however redshifted by roughly 30 nm. This reveals that the excitation of Ln^{2+} cannot fully account for the photo-oxidation process. It is therefore postulated that the additional broad band originates from the direct excitation of the filled hole trap, D^{Q+1}, which leads to the reversed electron transfer. To

further examine the spectral response of intrinsic and charge-compensating defects, the absorption difference spectra of the samples synthesized in air before and after 215 nm irradiation were obtained (see Figure S15). These spectra share some common features for the same host, irrespective of the type of dopants or doping. For phosphate compounds, the common hole trap is most likely formed by a pair of non-bridging oxygens bonded to the same phosphorus. This type of hole trap exhibits several characteristic absorption peaks centered around 300 nm, 420 nm and 500 nm.[38, 39] This is in line with what is observed here, especially for the sample doped with Gd (see Figure S15e) which requires a similar charge compensator as Eu, Yb and Sm-doped samples but shows no absorption features of Ln^{2+} in this wavelength range. Also, the absorption difference spectra can fully cover the wavelength-dependent oxidation spectra but with some difference in the relative effectiveness of different wavelengths. Here, it should be mentioned that the absorption difference spectrum is the combined result of the absorption from the D^{Q+1} and the Ln^{2+} ions, and might also include the absorption of some other defects that are not involved in the redox process. For the absorption difference spectrum of $Ba_{2.99}Eu_{0.01}(PO_4)_2$, the range between 300 nm and 400 nm can be ascribed to the absorption of Eu^{2+} as it matches the PLE spectrum of Eu^{2+} (see Figure 1a). Accordingly, the remaining features in the absorption difference spectrum can be linked either to the absorption of D^{Q+1} or to some other unrelated defects where there is no resemblance to the wavelength-dependent oxidation spectrum. Analogous conclusions can be drawn for the other compositions. In conclusion, it was found that the reverse oxidation process can be achieved through excitation of either the trapped electron from Ln^{2+} or the trapped hole from D^{Q+1}.

Subsequently, it was investigated to which extent the equilibrium between reduction and oxidation can be pushed in one direction for every wavelength. This was done by irradiating the sample for a time that is sufficiently long to ensure a (dynamic) equilibrium has set in. As shown in Figure 2c, the maximum reduction shows a similar behavior as the effectiveness, as a function of wavelength. For the photo-oxidation process (see Figure 2d), the maximum oxidation gradually enhances as the irradiation wavelength increases and the sample can be fully oxidized to its initial state when the irradiation wavelength is longer than a threshold wavelength. Although this wavelength varies for different compositions, it is close to the cut-off wavelength for the reduction process of the same composition. Upon irradiation below this wavelength, the two competing processes, namely, photo-oxidation and photo-reduction, co-exist and a dynamic equilibrium will be set upon sufficiently long time irradiation. This explains why the sample cannot be fully reduced or oxidized when irradiated by light within the overlap region of the oxidation spectrum and the reduction spectrum. Such a competition is also

observed in the coloring and bleaching of photochromic materials or the trapping and de-trapping of persistent luminescent materials.[40, 41]

2.3 Mechanism of photo-induced redox processes

The observed wavelength-dependent electron transfer processes in Ln-doped $Ba_3(PO_4)_2$ can be explained with a direct charge transfer mechanism,

$$Ln^{3+} + D^{Q} \underset{h\nu_2}{\overset{h\nu_1}{\rightleftarrows}} Ln^{2+} + D^{Q+1} \quad (1)$$

where the electron is directly transferred from a defect of unknown nature, denoted as D, to the lanthanide's valence shells. In this mechanism, the defect acts as a hole trap. In our experiments, photon energies $h\nu_1$ and $h\nu_2$ correspond to ultraviolet and visible light, respectively. As motivated above, it is sensible to assume that it is the charge compensator that can act as a hole trap. In that case equation (1) corresponds to a compensator-to-dopant charge transfer (CDCT).[42]

To substantiate equation (1), empirical CDCT configuration coordinate diagrams were constructed according to the method proposed in Ref. 43.[43] Input parameters are summarized in Table S2. For the energies of electronic excited states of $4f^{N-1}5d^1$ or LMCT nature, the measured excitation spectra were used as input. As it is very hard to reliably extract the first level of these rather dense electron configurations, it was estimated to be close to the low-energy tail of the excitation/absorption band. For the excited $4f^N$ levels, representative free-ion energy levels were taken. For the vertical offset between the ground state and charge transfer configurations, $E_{Ln^{2+}-D^{Q+1}}$, a value of 6000 cm^{-1} was chosen for the case of Eu^{3+}. From the known systematics in lanthanide-related charge transfer energies[44] and the assumption that the nature of the defect D is the same in all three cases, the energy differences between the LMCT configurations can be used for the differences in the vertical offset energies (see Table S2). Then, the magnitude of the average bond length change during process equation (1), Δd_{DA} is needed to quantify the horizontal offset between the ground state and charge transfer configurations. For this, a value of 0.15 Å is estimated, which is slightly lower than known data for lanthanide-to-lanthanide charge transfers in barium compounds[45], considering that a charge-compensating defect takes part in the process. Finally, the curvatures of the potential energy curves were determined from the vibrational frequency that enables the electronic transitions. For this, the lowest-energy totally symmetric mode as determined by vibrational spectroscopy, 602 cm^{-1}, was used.[46]

The resulting potential energy curves are displayed in **Figure 3**. Every curve shows the total energy of the relevant system, i.e. the lanthanide (Ln) center and the defect center (D) for

a specific electronic state. In these diagrams, the curves having their minimum at Q_{et} = 0 correspond to the initial state (left-hand side of equation (1)) and show the ground and excited states of the Ln^{3+} $4f^N$ configurations (colored curves). At higher energy, the LMCT manifold is found (grey color fill, an increased Eu-O equilibrium bond length was assumed for these states). For all these curves, the defect in charge state Q is considered to be in its electronic ground state (g.s.) and no low-lying excitations of D^Q are considered. The curves with a higher equilibrium $Q_{et} \approx 0.6$ Å value correspond to the CDCT configuration (right-hand side of equation (1)). Here, the states belonging to the $4f^N$ configurations are displayed as colored curves and the excited $4f^{N-1}5d^1$ configuration is shown as a violet color fill. Furthermore, the oxidized compensator, D^{Q+1}, has a low-lying excited state (e.s.) around 19200 cm^{-1}, displayed as the green curve. Only one discrete level is shown, however in reality it is possible that a denser band of energy levels is present.

From these diagrams, it is clear that upon excitation of the Ln^{3+} LMCT band (arrows 1), the stretched branch of the lowest CDCT state can be reached, enabling non-radiative relaxation towards the metastable CDCT configuration (arrows 2). As resonant Ln^{3+} $4f^N$ - $4f^N$ excitations at lower energies do not seem to result into the forward electron transfer, it looks as if the selected $E_{Ln^{2+}-D^{Q+1}}$ values are well in line with the experimental results, justifying their choice. For the optical re-oxidation process, there are two possibilities to induce the backward electron transfer. Firstly, the oxidized charge compensator can be excited by light absorption around 500 nm (arrows 3). The charge compensator is the same irrespective of the Ln^{3+} dopant, indeed giving rise to the same spectral feature in all cases (see Figure 2b). Secondly, the metastable Ln^{2+} ion can be excited via a $4f^N$-$4f^{N-1}5d^1$ transition of which the energy depends on the lanthanide (arrows 4). For Eu^{2+} and Yb^{2+}, the excitation energy is in the violet/near-ultraviolet, which is at higher energies than the absorption of the charge compensator. For Sm^{2+}, low-lying $4f^6$-$4f^5 5d^1$ absorptions occur, giving rise to an additional possibility to enable the electron back transfer at lower energies than the absorption of the charge compensator. After the photon absorption, the system relaxes non-radiatively to the initial state (arrows 5) or radiatively, via $4f^{N-1}5d^1$-$4f^N$ emission to the lowest CDCT state (arrow 4 reversed). The competition between both relaxation processes is determined by the details of the formed energy barrier and the transition rate for intersystem crossing, parameters that are not accessible in this simple empirical model. Apart from optical excitation, the re-oxidation process can be achieved upon thermal stimulation through arrows 6 (see Figure S16).

In conclusion, a direct compensator-to-defect charge transfer reasonably explains the experimental results. There is hence no need to assume the delocalization of charge carriers in

host-related valence or conduction band states. Given the large band gap energy of phosphates, it is indeed unlikely that these states play a role in visible-light-induced electron transfer processes. These findings can lead to much-needed insights regarding the photoinduced charge transfer process in luminescent materials.

Numerous optical devices are based on the luminescence of lanthanide activators. Typically, only one valence state is required to achieve a specific functionality. Multiple valence states can however occur simultaneously in those lanthanide doped phosphors, negatively affected the performance. This is the case for phosphor-converted LEDs and high-power fiber lasers, where the photo-induced valence change can degrade the quantum efficiency of the phosphors or increase the optical loss of the fiber[47, 48] This is caused by the intervalence charge transfer between Ln^{3+} and Ln^{2+}, which can provide a new non-radiative decay channel.[45, 49] In this sense, insight into the mechanism of photo-induced valence change of dopants is expected to provide guidelines for the development of other luminescent functional devices.

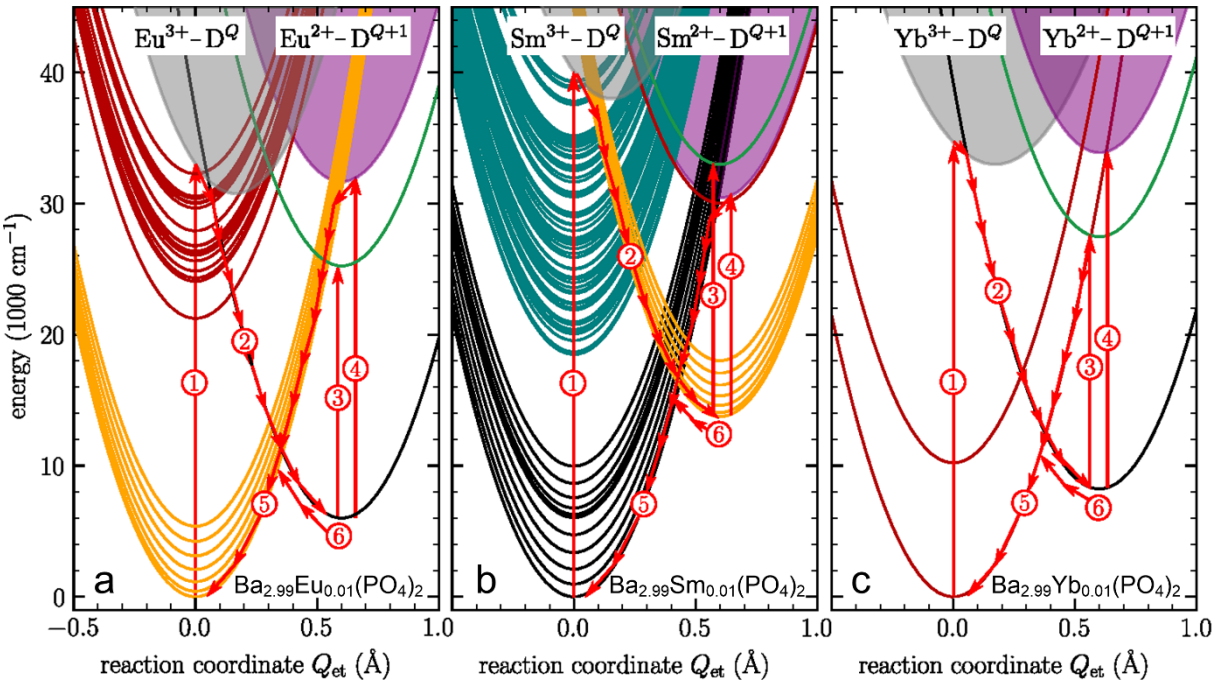

Figure 3. Photo-induced electron transfer processes. Compensator-to-dopant electron transfer configuration coordinate diagram for a) Eu^{3+}, b) Sm^{3+} and c) Yb^{3+} in $Ba_3(PO_4)_2$. Left: orange: $Eu^{3+}(4f^6(^7F_J))$ – D^Q(g.s.), maroon: $Eu^{3+}(4f^6(^5L_J))$ – D^Q(g.s.), grey: Eu^{3+}(LMCT) - D^Q(g.s.), black: $Eu^{2+}(4f^6(^8S_{7/2}))$ – D^{Q+1} (g.s.), violet: $Eu^{2+}(4f^65d^1)$ – D^{Q+1} (g.s.), green: $Eu^{2+}(4f^7(^8S_{7/2}))$ – D^{Q+1}(e.s.). Middle: black: Sm^{3+} $(4f^5(^6L_J))$ – D^Q (g.s.), turquoise: $Sm^{3+}(4f^5(^4L_J))$ – D^Q(g.s.), grey: Sm^{3+}(LMCT) – D^Q(g.s.), orange: $Sm^{2+}(4f^6(^7F_J))$ – D^{Q+1}(g.s.), maroon: $Sm^{2+}(4f^6(^5D_0))$ – D^{Q+1}(g.s.), violet: $Sm^{2+}(4f^55d^1)$ – D^{Q+1}(g.s.), green: $Sm^{2+}(4f^6(^7F_0))$ – D^{Q+1}(e.s.). Right: maroon: $Yb^{3+}(4f^{13}(^2F_J))$ – D^Q(g.s.), grey: Yb^{3+}(LMCT) – D^Q (g.s.), black: $Yb^{2+}(4f^{14}(^1S_0))$ – D^{Q+1}(g.s.),

violet: $Yb^{2+}(4f^{13}5d^{1}) – D^{Q+1}$(g.s.), green: $Yb^{2+}(4f^{14}(^{1}S_{0})) – D^{Q+1}$(e.s.). The numbered transitions are explained in the text.

2.4. Wavelength-specific Light Dosimeters for Personal Solar Ultraviolet Monitoring

The results of photo-induced redox processes indicate that the dose and wavelength dependency of reduction and oxidation process can be utilized for selective ultraviolet and visible light dosimetry. Currently, polysulphone materials are still commercially used for personal solar ultraviolet dosimetry, even if their wavelength response does not fully match the erythemal action spectrum of human skin (see **Figure 4a**).[9] This leads to a complex and error-prone calibration process.[31] Encouragingly, the wavelength dependent reduction behavior found in $Ba_{2.99}Eu_{0.01}(PO_4)_2$ much better matches the erythemal action spectrum (see Figure 4a). This motivated us to further evaluate the possibility of $Ba_{2.99}Eu_{0.01}(PO_4)_2$ as a personal solar ultraviolet radiation dosimeter. The dose-dependent responsive behavior of $Ba_{2.99}Eu_{0.01}(PO_4)_2$ under an ultraviolet irradiation source (Figure S17) that covers the wavelength range to induce the erythema was investigated (see Figure 4b). Monotonic dose response is observed in $Ba_{2.99}Eu_{0.01}(PO_4)_2$ dosimeters with a more sensitive response in the low dose range (see Figure 4c). Upon further irradiation, the response gradually reaches saturation, corresponding to an integrated dose around 1200 mJ cm^{-2}. Here, the range with high sensitivity (0-200 mJ cm^{-2}) can perfectly cover the minimal erythemal doses of different skin types,[14] and repeated tests show a good reproducibility of the dosimeter (Figure S18). Meanwhile, the sensitivity achieved in $Ba_{2.99}Eu_{0.01}(PO_4)_2$ in that dose range is higher than that of commercially used polysulphone-based dosimeters.[9] For dosimetry, it is also required that the response of the dosimeter is independent of the irradiation intensity. Put differently, the response under a short exposure time of a light source with a high intensity should be the same as the result under a long exposure time of a light source with a low intensity. As shown in Figure 4d, the response of $Ba_{2.99}Eu_{0.01}(PO_4)_2$ is intensity-independent, which enables the dosimeter to monitor the irradiation source with large variations in intensity.

In addition to the dose-response behavior, the stability and cycling robustness should be considered as well for practical dosimetry. The fading characteristic was tested by continuously measuring the PL spectra after 265 nm irradiation and then waiting for different durations (red dot in Figure 4e). The signal attenuates quickly at the initial stage and fades around 40 % in 72 h. Here, it should be mentioned that the continuous readout process is responsible for a partial fading of the signal as the excitation source can also induce the oxidation effect. To exclude this effect, the signal was read out directly after waiting in the dark for 24 h or 48 h after irradiation. As shown in Figure 4e (red square), the signal intensity of waiting for 24 h and

waiting for 48 h is nearly the same, indicating that the signal has stabilized after 24 h with an intrinsic fading of less than 20 % within 48 h. Finally, the sample exhibits excellent cycling robustness upon alternate 265 nm and 420 nm irradiation (see Figure 4f), which guarantees that the dosimeter can be reused.

If the dose information is required to be read out by detecting the absolute photoluminescence intensity of either Eu^{2+} or Eu^{3+}, a stable excitation source is needed, which is not convenient for practical dosimetry. A further look at the PLE spectra in Figure 1a indicates that Eu^{2+} and Eu^{3+} ions can be excited simultaneously at specific wavelengths. This makes the dose readout process possible by detecting the luminescence intensity ratio between Eu^{2+} and Eu^{3+} in a ratiometric way, thereby relaxing the strict requirement of the excitation source. As shown in Figure 4g, the read-out value is indeed independent of the intensity of the excitation source. Thanks to the significant difference in photoluminescence spectrum between Eu^{2+} and Eu^{3+}, there is a dose-dependent photoluminescence color change (see Figure 4h), which supports an on-site assessment of doses by direct visual or camera-assisted inspection. This dosimetry method can remove the requirement for expensive, spectrally-resolved readout instruments and is attractive for consumer-based dosimetry.

With the variation of the dopant from Eu to Sm and Yb or the host from $Ba_3(PO_4)_2$ to $Sr_3(PO_4)_2$, the wavelength-dependent reduction or oxidation behavior changes accordingly (see Figure 2a and 2b), which can also be utilized for dosimetry in certain applications. This is for example the case of phototherapy for neonatal jaundice where the oxidation process of $Sr_{2.99}Sm_{0.01}(PO_4)_2$ exhibits a similar wavelength response as the absorbance spectrum of bilirubin bound to human serum albumin.[11] Also, the dosimetry properties of $Sr_{2.99}Sm_{0.01}(PO_4)_2$ show good stability with an intrinsic fading of less than 9 % within 48 h and excellent cycling robustness (Figure S19). In addition, the approach proposed here allows the development of dosimeters with other specific responsive behavior by further tuning the chemical composition from phosphate compounds to silicate or sulfate compounds where the photo-induced redox behavior can also be expected.

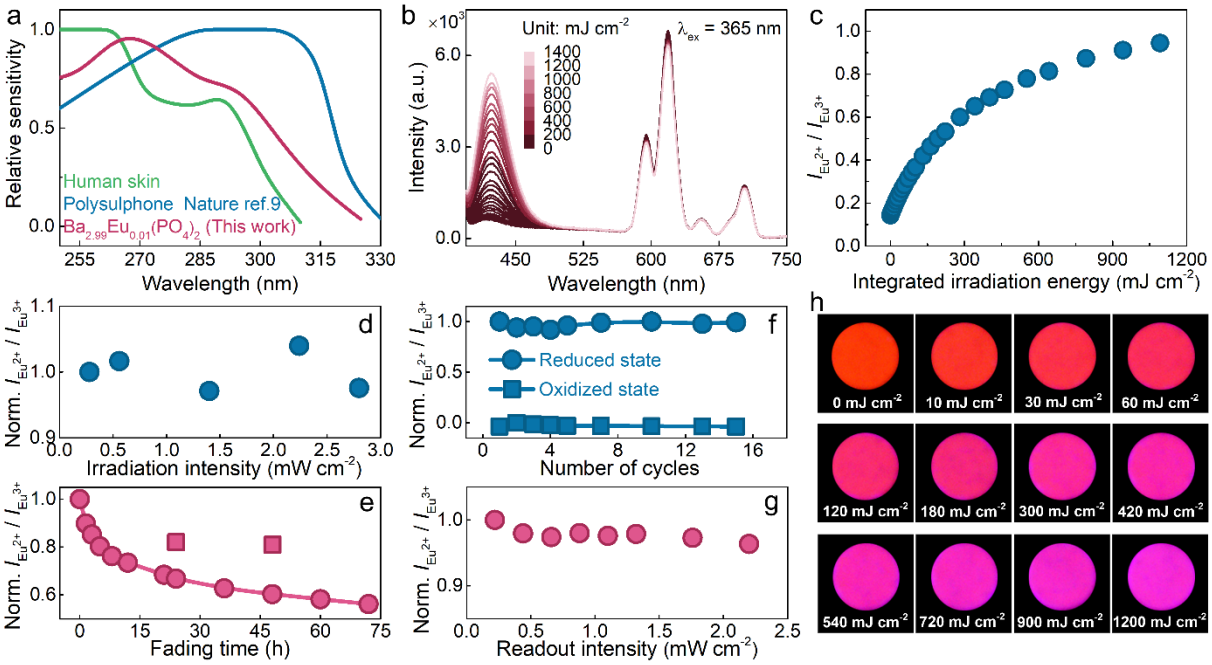

Figure 4. Performance of wavelength-specific dosimetry. a) Wavelength-dependent responsive behavior of polysulphone and $Ba_{2.99}Eu_{0.01}(PO_4)_2$ and the erythemal action spectrum of human skin. b) Photoluminescence emission spectra (λ_{ex} = 365 nm) of $Ba_{2.99}Eu_{0.01}(PO_4)_2$ as a function of irradiation energy of the ultraviolet light source. c) Dose dependency of $I_{Eu^{2+}}/I_{Eu^{3+}}$ after illuminating different doses of ultraviolet light. d) Effect of the irradiation intensity on the response of $I_{Eu^{2+}}/I_{Eu^{3+}}$. e) Fading characteristics of $Ba_{2.99}Eu_{0.01}(PO_4)_2$. The circles represent the signal intensity that was continuously measured after irradiation and then waiting different durations. The squares represent the signal intensity that was measured by direct waiting for certain durations after irradiation. f) Cycling performance of $Ba_{2.99}Eu_{0.01}(PO_4)_2$. g) Effect of the readout intensity on the value of $I_{Eu^{2+}}/I_{Eu^{3+}}$. h) Photographs of $Ba_{2.99}Eu_{0.01}(PO_4)_2$ synthesized in air upon the ultraviolet light source irradiation with different doses.

3. Conclusion

In this work, we demonstrate an approach to develop wavelength-specific integrating light dosimeters based on the photo-induced reversible valence change of lanthanide dopants in luminescent materials. Spectroscopy experiments reveal that the photo-reduction process can be achieved through excitation of the ligand-to-metal charge transfer manifold while the photo-oxidation process can be realized upon excitation of the involved hole traps or via $4f^N$-$4f^{N-1}5d^1$ excitation of the induced divalent lanthanide dopants. Guided by this approach, an ideal dosimeter for personal solar ultraviolet monitor is obtained in $Ba_{2.99}Eu_{0.01}(PO_4)_2$, which exhibits a better matched response spectrum and a higher dose sensitivity compared to the commercially available polysulphone-based dosimeters. Meanwhile, thanks to the distinct luminescence

spectra of Eu^{3+} and Eu^{2+}, an irradiation-dose-dependent photoluminescence color shift was obtained in $Ba_{2.99}Eu_{0.01}(PO_4)_2$. This characteristic allows on-site assessment of doses via a colorimetric method without the need for any special instruments, which is attractive for consumer-based daily dosimetry. These results confirm the feasibility of the proposed method, which opens a new window to design spectrally selective dosimeters using the intrinsic response property of the material. It also makes it possible to develop specific dosimeters for envisioned applications as a specific wavelength sensitivity can be obtained by changing the composition of the host or of the lanthanide ion. Moreover, the provided in-depth understanding of the photo-induced charge transfer mechanism is expected to provide guidelines for developing other luminescent functional devices.

4. Experimental Section

Sample Preparation: The samples of $Ba_3(PO_4)_2$, $Ba_{2.99}Ln_{0.01}(PO_4)_2$ (Ln = Eu, Sm, Yb, or Gd) and $Sr_{2.99}Sm_{0.01}(PO_4)_2$ were synthesized via a solid-state reaction method using $BaCO_3$ (Alfa Aesar, 99.8%), $SrCO_3$ (Sigma Aldrich, 99.9%), $(NH_4)_2HPO_4$ (Sigma Aldrich, 98%), Eu_2O_3 (Alfa Aesar, 99.99%) Sm_2O_3 (Alfa Aesar, 99.99%) and YbF_3 (Alfa Aesar, 99.9%) as raw materials without further purification. The raw materials were weighed stoichiometrically followed by ball milling with ethanol for 5 h at a rotation speed of 300 rpm. The mixed powders were first dried in an oven at 60 °C for 8 h and then calcined at 300 °C for 5 h. The obtained powders were mixed with a polyvinyl alcohol binder solution (5 wt.%) and pressed into pellets with a thickness of around 1 mm and a diameter of 13 mm. Finally, the pellets were sintered at 1300 °C for 5 h with a heating rate of 300 °C/h and in different atmospheres (air or 90% N_2+10% H_2) to obtain dense ceramics. It should be mentioned that the synthesis process of $Ba_{2.99}Eu_{0.01}(PO_4)_2$ was optimized to ensure that the Eu ions are in their trivalent state in the synthesized sample. Compared to other compositions, the mixed powder of $Ba_{2.99}Eu_{0.01}(PO_4)_2$ was only dried in an oven at 60 °C for 24 h without further calcination. In addition, the prepared pellets of $Ba_{2.99}Eu_{0.01}(PO_4)_2$ were first calcined at 950 °C for 5 h and then sintered at 1300 °C for 5 h.

Characterization: The phase purity of synthesized samples was checked with X-ray diffraction using a Siemens D5000 diffractometer (40 kV, 40 mA) with Cu $K_{\alpha 1}$ radiation (λ = 0.154 nm) (Figure S20). Room-temperature photoluminescence emission (PL) spectra and photoluminescence excitation (PLE) spectra were obtained on an Edinburgh FS920 fluorescence spectrometer, using a 450 W xenon arc lamp as excitation source and equipped with a Hamamatsu R928P red-sensitive photomultiplier for 200 - 850 nm detection and a Ge IR detector for 700 -1600 nm detection. The same spectrometer equipped with a cryostat

(Oxford Instruments Optistat CF) was used to measure the low-temperature PL spectrum of $Ba_{2.99}Eu_{0.01}(PO_4)_2$. The VUV charge transfer bands of $Ba_{2.99}Eu_{0.01}(PO_4)_2$, $Ba_{2.99}Sm_{0.01}(PO_4)_2$ and $Sr_{2.99}Sm_{0.01}(PO_4)_2$ were determined using a modified Edinburgh Instrument FL920, for which the VUV excitation arm consists of a D_2 lamp (DS-775), an Acton Research VM-504 monochromator, and a mirror based focusing unit. The focusing unit and the interior of the monochromator are set under a vacuum of 5×10^{-5} mbar by using a turbo molecular pump. The sample chamber itself is continuously flushed by dried nitrogen gas (99.999 %). The excitation spectrum of $Ba_{2.99}Yb_{0.01}(PO_4)_2$ monitored for the ultraviolet band was measured by a combination of a OPO laser and a near-infrared spectrometer of AvaSpec-NIR512-1.7-HSC-EVO.

To perform the photo-induced reversible valence change of the dopants, a home-made setup was employed (Figure S21), in which two shutters were controlled by a LabVIEW program to alternately block and open the irradiation source and the excitation source. In combination with a NT340 series tunable OPO laser (EKSPLA, Lithuania), the setup allows us to perform the wavelength-dependent reduction and oxidation processes of the dopants. During measurements, the PL spectra were recorded using a QE65000 array spectrometer (Ocean Optics) under the excitation of 365 nm LED (FWHM = 16 nm) or 420 nm LED (FWHM = 20 nm). A pyroelectric energy sensor (ES220C, Thorlabs) was employed to measure the energy of the laser pulse of different wavelengths. For the reduction experiments, the sample was pre-irradiated for 1 h (340 nm for $Ba_{2.99}Eu_{0.01}(PO_4)_2$, 420 nm for $Ba_{2.99}Yb_{0.01}(PO_4)_2$, $Ba_{2.99}Sm_{0.01}(PO_4)_2$ and $Sr_{2.99}Sm_{0.01}(PO_4)_2$) to reach the same oxidation state. Similarly, for the photo-oxidation experiment at each wavelength, the sample was first illuminated for 30 min (265 nm for $Ba_{2.99}Eu_{0.01}(PO_4)_2$, 235 nm for $Ba_{2.99}Yb_{0.01}(PO_4)_2$, 225 nm for $Ba_{2.99}Sm_{0.01}(PO_4)_2$ and 220 nm for $Sr_{2.99}Sm_{0.01}(PO_4)_2$) to ensure that the formed Ln^{2+} ions are at the same level of saturation. The effectiveness of different wavelengths for the reduction process was determined under illumination with doses of 35 mJ, 60 mJ, 60 mJ and 60 mJ for $Ba_{2.99}Eu_{0.01}(PO_4)_2$, $Ba_{2.99}Yb_{0.01}(PO_4)_2$, $Ba_{2.99}Sm_{0.01}(PO_4)_2$ and $Sr_{2.99}Sm_{0.01}(PO_4)_2$, respectively. The effectiveness of different wavelengths for the oxidation process was determined under illumination with doses of 350 mJ, 150 mJ, 600 mJ and 350 mJ for $Ba_{2.99}Eu_{0.01}(PO_4)_2$, $Ba_{2.99}Yb_{0.01}(PO_4)_2$, $Ba_{2.99}Sm_{0.01}(PO_4)_2$ and $Sr_{2.99}Sm_{0.01}(PO_4)_2$, respectively. To obtain the wavelength-dependent maximum reduction/oxidation state, the samples were irradiated for 40 min at every wavelength for the reduction process, while the irradiation time was in the range of 1 h to 5 h for the oxidation process at every wavelength, depending on the effectiveness.

EPR measurements were performed at room temperature on a Bruker ElexSys E500 spectrometer operating at Q-band (34 GHz) equipped with a Pendulum CNT-90XL frequency counter for the microwave frequency measurement and a Bruker NMR ER 035M Gaussmeter for the magnetic field measurement. Diffuse reflectance spectra were measured on a PerkinElmer Lambda 1050 UV-vis-NIR spectrophotometer equipped with a Spectralon-coated integrating sphere with photomultiplier and InGaAs detectors. The obtained spectra were converted to absorption spectra based on the Kubelka-Munk model.[50] Thermal oxidation experiments were carried out by consecutively annealing the initially maximally reduced samples in air at different temperatures for 5 min in an ascending order. The dose-dependent response curve was obtained using the same home-made setup using an ultraviolet LED as light source (see Figure S17 for the spectrum). The irradiation-intensity-dependent response behavior was assessed by changing the intensity of the light source and the exposure time but ensuring that the same integrated dose is reached. An S401C thermal power sensor coupled to a PM100 readout unit (Thorlabs) was employed to measure the power density of the light source. Photographs were taken with a Nikon D3200 camera (Nikon Corporation; Japan) in raw format under a fixed exposure time of 1/20 s and ISO of 6400. The 365 nm LED (FWHM = 16 nm) was used as the illumination source for taking the photographs.

Supporting Information

Supporting Information is available from the Wiley Online Library or from the author.

Acknowledgements

The authors acknowledge the financial support from the FWO (Fund for Scientific Research-Flanders, projects I002418N and G0F9322N).

Conflict of Interest

The authors declare no conflict of interest.

Data availability

The data that support the findings of this study are available from the corresponding author upon reasonable request.

Received: ()
Revised: ()
Published online: ()

References

[1] Z.H. Bian, Q.C. Yang, W.K. Liu, *J. Sci. Food Agric.* **2015**, *95*, 869.
[2] U.V. Pedmale, S.C. Huang, M. Zander, B.J. Cole, J. Hetzel, K. Ljung, P.A.B. Reis, P. Sridevi, K. Nito, J.R. Nery, J.R. Ecker, J. Chory, *Cell* **2016**, *164*, 233.
[3] R. Marin, E. Ximendes, D. Jaque, *Light: Sci. Appl.* **2022**, *11*, 65.
[4] M. Buonanno, D. Welch, I. Shuryak, D.J. Brenner, *Sci. Rep.* **2020**, *10*, 10285.
[5] M. Wacker, M.F. Holick, *Dermatoendocrinol.* **2013**, *5*, 51.
[6] A.T. Slominski, M.A. Zmijewski, P.M. Plonka, J.P. Szaflarski, R. Paus, *Endocrinology* **2018**, *159*, 1992.
[7] S. Madronlch, F.R.d. Gruiji, *Nature* **1993**, *386*, 23.
[8] J. D'Orazio, S. Jarrett, A. Amaro-Ortiz, T. Scott, *Int. J. Mol. Sci.* **2013**, *14*, 12222.
[9] A. Davis, G.H.W. Deane, B.L. Diffey, *Nature* **1976**, *261*, 169.
[10] R. Dang, B. Wang, X. Song, F. Zhang, G. Liu, *Sci. Rep.* **2021**, *11*, 10951.
[11] M.J. Maisels, A.F. McDonagh, *N. Engl. J. Med.* **2008**, *358*, 920.
[12] M.D. Ooms, C.T. Dinh, E.H. Sargent, D. Sinton, *Nat. Commun.* **2016**, *7*, 12699.
[13] S. Dhanekar, K. Rangra, *Adv. Mater. Technol.* **2021**, *6*, 2000895.
[14] W. Zou, M. Sastry, J.J. Gooding, R. Ramanathan, V. Bansal, *Adv. Mater. Technol.* **2020**, *5*, 1901036.
[15] E.G. Yukihara, S.W.S. McKeever, C.E. Andersen, A.J.J. Bos, I.K. Bailiff, E.M. Yoshimura, G.O. Sawakuchi, L. Bossin, J.B. Christensen, *Nat. Rev. Methods Primers* **2022**, *2*, 26.
[16] A. Saha, G. Kumar, S. Pradhan, G. Dash, R. Viswanathab, G. Konstantatos, *Adv. Mater.* **2022**, *34*, 2109498.
[17] J. Michel, J. Liu, L.C. Kimerling, *Nature Photon.* **2010**, *4*, 527.
[18] X. Liu, L. Gu, Q. Zhang, J. Wu, Y. Long, Z. Fan, *Nat. Commun.* **2014**, *5*, 4007.
[19] S.Y. Heo, J. Kim, P. Gutruf, A. Banks, P. Wei, R. Pielak, G. Balooch, Y. Shi, H. Araki, D. Rollo, C. Gaede, M. Patel, J.W. Kwak, A.E. Peña-Alcántara, K.-T. Lee, Y. Yun, J.K. Robinson, S. Xu, J.A. Rogers, *Sci. Transl. Med.* **2018**, *10*, eaau1643.
[20] K. Kwon, S.Y. Heo, I. Yoo, A. Banks, M. Chan, J.Y. Lee, J.B. Park, J. Kim, J.A. Rogers, *Sci. Adv.* **2019**, *5*, eaay2462.
[21] X. Xu, J. Chen, S. Cai, Z. Long, Y. Zhang, L. Su, S. He, C. Tang, P. Liu, H. Peng, X. Fang, *Adv. Mater.* **2018**, *30*, 1803165.
[22] S. Cai, C. Zuo, J. Zhang, H. Liu, X. Fang, *Adv. Funct. Mater.* **2021**, *31*, 2100026.
[23] Z. Wang, Y. Wang, Z. Ge, Y. Tian, M. Ai, S. Cao, M. Wang, S. Wang, J. Ma, *Matter* **2022**, *11*, 4060.
[24] H. Lu, J. Xie, X.Y. Wang, Y. Wang, Z.J. Li, K. Diefenbach, Q.J. Pan, Y. Qian, J.Q. Wang, S. Wang, J. Lin, *Nat. Commun.* **2021**, *12*, 2798.
[25] W. Zou, A. Gonzalez, D. Jampaiah, R. Ramanathan, M. Taha, S. Walia, S. Sriram, M. Bhaskaran, J.M. Dominguez-Vera, V. Bansal, *Nat. Commun.* **2018**, *9*, 3743.
[26] I. Norrbo, A. Curutchet, A. Kuusisto, J. Mäkelä, P. Laukkanen, P. Paturi, T. Laihinen, J. Sinkkonen, E. Wetterskog, F. Mamedov, T. Le Bahers, M. Lastusaari, *Mater. Horiz.* **2018**, *5*, 569.
[27] K. Pushpavanam, S. Inamdar, S. Dutta, T. Bista, T. Sokolowski, E. Boshoven, S. Sapareto, K. Rege, *Sci. Adv.* **2019**, *5*, eaaw8704.

[28] H. Lu, H. Hou, Y.C. Hou, Z. Zheng, Y. Ma, Z. Zhou, X. Guo, Q.J. Pan, Y. Wang, Y. Qian, J.Q. Wang, J. Lin, *J. Am. Chem. Soc.* **2022**, *144*, 3449.
[29] X. Wang, X. Chen, D. Zhang, J. Chen, P. Deng, Z. Zhong, Q. Xiang, J. Li, F. Li, Y. Liao, *ACS Sens.* **2019**, *4*, 2429.
[30] D. Van der Heggen, R. Zilenaite, E. Ezerskyte, V. Fritz, K. Korthout, D. Vandenberghe, J. De Grave, J. Garrevoet, L. Vincze, D. Poelman, J.J. Joos, P.F. Smet, *Adv. Funct. Mater.* **2021**, *32*, 2109635.
[31] B. Diffey, *Atmosphere* **2020**, *11*, 125.
[32] J.J. Joos, D. Van der Heggen, L. Amidani, L. Seijo, Z. Barandiarán, *Phys. Rev. B* **2021**, *104*, L201108.
[33] Z. Yang, J. Hu, D. Van der Heggen, A. Feng, H. Hu, H. Vrielinck, P.F. Smet, D. Poelman, *Adv. Funct. Mater.* **2022**, *32*, 2201684.
[34] H. Liang, Y. Tao, Q. Su, S. Wang, *J. Solid State Chem.* **2002**, *167*, 435.
[35] K. Sugiyama, M. Tokonami, *Mineral. J.* **1990**, *15*, 141.
[36] E.S. Sabisky, *J. Appl. Phys.* **1965**, *36*, 1788.
[37] P.A. Tanner, *Chem. Soc. Rev.* **2013**, *42*, 5090.
[38] D.L. Griscom, E.J. Friebele, K.J. Long, J.W. Fleming, *J. Appl. Phys.* **1983**, *54*, 3743.
[39] P. Ebeling, D. Ehrt, M. Friedrich, *Opt. Mater.* **2002**, *20*, 101.
[40] D. Van der Heggen, J.J. Joos, P.F. Smet, *ACS Photonics* **2018**, *5*, 4529.
[41] Z. Yang, J. Hu, D. Van der Heggen, M. Jiao, A. Feng, H. Vrielinck, P.F. Smet, D. Poelman, *Laser Photonics Rev.* **2023**, DOI: 10.1002/lpor.202200809.
[42] C. MacKeen, F. Bridges, L. Seijo, Z. Barandiarán, M. Kozina, A. Mehta, M.F. Reid, J.P.R. Wells, *J. Phys. Chem. C* **2017**, *121*, 28435.
[43] Z. Barandiaran, A. Meijerink, L. Seijo, *Phys. Chem. Chem. Phys.* **2015**, *17*, 19874.
[44] J.J. Joos, I. Neefjes, L. Seijo, Z. Barandiaran, *J. Chem. Phys.* **2021**, *154*, 064704.
[45] I. Neefjes, J.J. Joos, Z. Barandiarán, L. Seijo, *J. Phys. Chem. C* **2020**, *124*, 2619.
[46] M.E. Poloznikova, V.V. Fomichev, *Russ. Chem. Rev.* **1994**, *63*, 399.
[47] M.A. van de Haar, M. Tachikirt, A.C. Berends, M.R. Krames, A. Meijerink, F.T. Rabouw, *ACS Photonics* **2021**, *8*, 1784.
[48] M.M. Broer, D.M. Krol, D.J. DiGiovanni, *Opt. Lett.* **1993**, *18*, 799.
[49] J.J. Joos, L. Seijo, Z. Barandiaran, *J. Phys. Chem. Lett.* **2019**, *10*, 1581.
[50] P. Kubelka, F. Munk, *Z. Technol. Phys.* **1931**, *12*, 593.

Z. Yang, J. J. Joos,* J. Hu, D. Van der Heggen,* T. Pier, M. Delaey, H. Vrielinck, T. Jüstel, P. F. Smet, and D. Poelman*

Tailoring Phosphor-Based Light Dosimeters to Match the Spectral Sensitivity for Personal Solar Ultraviolet Monitoring

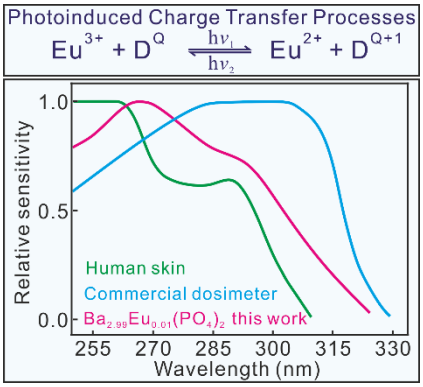

Based on the in-depth understanding of the photoinduced charge transfer processes in luminescent materials, an ideal light dosimeter for personal solar ultraviolet monitor is obtained in $Ba_{2.99}Eu_{0.01}(PO_4)_2$, which exhibits a better matched response spectrum and a higher sensitivity compared to currently-used benchmark polysulphone dosimeters. This opens the door to design wavelength-specific light dosimeters according to the requirements of envisioned applications.